

2014-01-01

Characterization Of W-Ti-O Thin Films For Application In Photovoltaics

Amanda Patricia Christmas

University of Texas at El Paso, apgutierrez@miners.utep.edu

Follow this and additional works at: https://digitalcommons.utep.edu/open_etd



Part of the [Materials Science and Engineering Commons](#), and the [Mechanics of Materials Commons](#)

Recommended Citation

Christmas, Amanda Patricia, "Characterization Of W-Ti-O Thin Films For Application In Photovoltaics" (2014). *Open Access Theses & Dissertations*. 1219.

https://digitalcommons.utep.edu/open_etd/1219

This is brought to you for free and open access by DigitalCommons@UTEP. It has been accepted for inclusion in Open Access Theses & Dissertations by an authorized administrator of DigitalCommons@UTEP. For more information, please contact lweber@utep.edu.

CHARACTERIZATION OF W-Ti-O THIN FILMS FOR APPLICATION IN
PHOTOVOLTAICS

AMANDA P. CHRISTMAS

Department of Metallurgical and Materials Engineering

Approved:

Chintalapalle V. Ramana, Ph.D., Chair

Stephen W. Stafford, Ph.D.

Peter Golding, Ph.D.

Charles Ambler, Ph.D.
Dean of the Graduate School

Copyright ©

by

Amanda P. Christmas

2014

CHARACTERIZATION OF W-Ti-O THIN FILMS FOR APPLICATION IN
PHOTOVOLTAICS

by

AMANDA P. CHRISTMAS, B.S.M.M.E

THESIS

Presented to the Faculty of the Graduate School of

The University of Texas at El Paso

in Partial Fulfillment

of the Requirements

for the Degree of

Master of Science

Department of Metallurgical and Materials Engineering

THE UNIVERSITY OF TEXAS AT EL PASO

August 2014

Acknowledgements

I would like to thank Dr. C.V. Ramana my advisor for his dedication and willingness to not give up on me. He is a great advisor and has an abundance of knowledge. Dr. Ramana is a wonderful person and I feel truly honored to be a part of his research group. I would also like to thank Dr. Peter Golding and Dr. Stephen Stafford for agreeing to be on my graduate committee and for their never ending support. I am thankful for the facilities and instruments available for my use at The University of Texas at El Paso.

I dedicate my thesis to my grandfather “Pa” Frank J. Anaya, my family and my husband Matt Christmas. I would like to thank my mother and family for their continuous support and motivation which has carried me through my educational experience. My husband has been my inspiration through graduate school and has done nothing but push and cheer me on every step of the way. I am very fortunate and lucky to have loved ones with such great desire to see me succeed in life. Last but definitely not least I must thank the great Lord because nothing is impossible through Him.

Abstract

Photovoltaic (PV) devices consist of the conversion of light energy into electricity. Nearly all PV technologies employ transparent conducting oxides (TCO) as an integral part of the device structure so that the light can reach the semiconductor. The predominant transparent conducting oxide (TCO) that is currently being used in industry is indium tin oxide (ITO). However, Indium (In) is high in cost and becoming scarce in the world. This work is focused towards Titanium doped Tungsten oxide (WO_3) for TCO application. The ultimate goal is making novel, cheaper, and efficient TCOs based on W-Ti-O films. Titanium will enhance the conductivity of the film. In addition, Ti is more abundant than In thus leading to low-cost TCO. Ti-doped WO_3 (W-Ti-O) films were grown by co-sputter deposition onto silicon, Si (100), and optical grade quartz wafers. Co-sputtering of Ti and W metal targets was performed in a wide growth temperature range (room temperature (RT)-500 °C). The Ti sputtering power varied from 50 watts-100 watts in order to gain an understanding of the Ti effect. The structure and optical properties were characterized by the X-ray diffraction (XRD), scanning electron microscopy (SEM) and the spectrophotometry measurements. The films are optically transparent and a correlation between the growth conditions and optical properties is derived. The XRD results show W-Ti-O films grown at RT are amorphous and the films crystallize at 200°C. A decrease in the peak intensity implies that the crystallinity decreases with an increase in titanium (Ti) along with a phase change at higher substrate growth temperatures. The optical results show the transparency of the films is well above 80%. The energy band gap decreases from 4.0 eV to 3.9 eV with an increase in substrate temperature and increases from 3.85 eV to 3.95 eV with an increase of Ti. These results meet the criteria of two essential TCO parameters.

Table of Contents

Acknowledgements	iv
Abstract	v
List of Tables	vii
List of Figures	viii
Chapter 1: Introduction	1
1.1 Thin Films	3
1.2 Transparent Conducting Oxides (TCO) and Photovoltaics (PV)	3
1.3 Tungsten Oxide (WO ₃)	5
1.4 Titanium Doping	9
Chapter 2: Experimental Methods	13
3.1 Physical Vapor Deposition and Sputter Deposition	13
3.2 Characterization	16
3.2.1 X-Ray Diffraction	16
3.2.2 Scanning Electron Microscopy	18
3.3 Optical Analyses	19
3.3.1 Energy Band Gap (E _g)	20
Chapter 3: Results and Discussions	23
3.1 XRD Results	23
4.2 SEM Results	25
4.3 Optical Results	26
Chapter 4: Conclusions	30
Chapter 5: Future Work	32
References	33
Curriculum Vita	37

List of Tables

Table 1. Common ITO properties.....	5
Table 2. Effect of temperature -WO ₃ grown films.....	15
Table 3. Effect of increasing Ti sputtering power - WO ₃ grown films.	15

List of Figures

Figure 1. Layers of a thin film used for PV devices	2
Figure 2. Assembly of a basic photovoltaic device.	4
Figure 3. ReO ₃ -type Perovskite WO ₃ Structure [56-58].	6
Figure 4. WO ₃ layers create tunneling for ion transport [56-58].	7
Figure 5. WO ₃ polymorphism	8
Figure 6. XRD pattern of WO ₃ films grown at various temperatures [20].....	9
Figure 7. Phase diagram summarizing the microstructure evolution of W _{0.95} Ti _{0.05} O ₃ films as a function of temperature [14].	11
Figure 8. Variation in electrical conductivity of W _{0.95} Ti _{0.05} O ₃ films with substrate temperature [14].....	12
Figure 9. Co-sputter deposition using Ti and W metal targets.	13
Figure 10. Bruker D8 Advance X-ray diffractometer.....	16
Figure 11. Bragg's law through X-ray diffraction.	17
Figure 12. Hitachi S-4800 Scanning Electron Microscope (SEM).....	18
Figure 13. Cary 5000 UV-VIS-NIR optical spectrometer	19
Figure 14. Explanation of band gap [53]	20
Figure 15. Indirect band gap [54].	21
Figure 17. XRD patterns of co-sputtered W-Ti-O films grown at different Ti-target sputtering powers.	23
Figure 16. XRD patterns of co-sputtered W-Ti-O films grown at various temperatures.	24
Figure 18. The high-resolution SEM images of W-Ti-O films with a sputtering power of Ti-target at 50W as a function of substrate temperature.....	26

Figure 19. The high-resolution SEM images of W-Ti-O films as a function of Ti-target sputtering power.....	26
Figure 20. Optical transmittance spectra of W-Ti-O films with a sputtering power of Ti-target at 50W as a function of substrate temperature.....	27
Figure 21. Optical transmittance spectra of W-Ti-O films as a function of Ti-target sputtering power.....	27
Figure 22. Absorption data of W-Ti-O with a sputtering power of Ti-target at 50W as a function of substrate temperature.....	28
Figure 23. Absorption data of W-Ti-O as a function of Ti-target sputtering power.	29
Figure 24. $(\alpha h\nu)^{1/2}$ vs $h\nu$ plots for W-Ti-O films grown at various Ti-target sputtering power. Extrapolating the linear region of the plot to $h\nu=0$ provides the band gap value.	30

Chapter 1: Introduction

Photovoltaic (PV) devices are becoming the world's main supply of energy source giving the economy jobs and sustainability at a high production and low cost rate. Photovoltaic devices convert light energy into electricity by utilizing the “photo-voltaic” effect. The three main processes or key functions of a PV device are: (1) the absorption of light, generating either electron-hole pairs or excitons; (2) the separation of charge carriers; and (3) the extraction of the charge carriers to produce electricity.

The PV device consists of a multilayer stack, which will be able to perform the key functions [1]. Transparent conducting oxides (TCO) are conductive and optically transparent thin films used for application in photovoltaics. Nearly all PV technologies employ TCOs as an integral part of the basic device structure [1]. TCOs utilized as photovoltaic (PV) devices have been extensively investigated since these devices are rather easy to manufacture, inexpensive, transparent, light and flexible. As shown in Figure 1, the TCO material is an important component of a PV device, where it acts as an electrode element, structure template and diffusion barriers [1]. An alternate strategy that is employed in the solar industry in the construction of PV solar cells is to use layers of different materials coated onto a silicon base material. The metal thickness of the TCO is an important characteristic since it has the ability to improve the transmittance to 80% due to the reduction of the reflectance occurring at the interfaces.

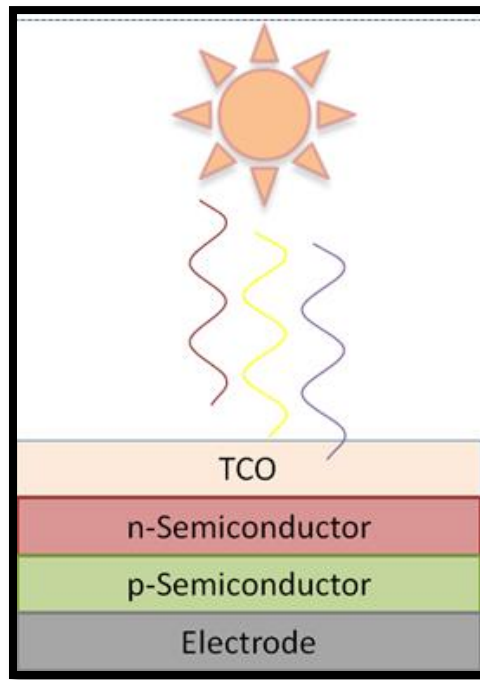


Figure 1. Layers of a thin film used for PV devices

The industry standard TCO today is based on indium tin oxide (ITO). However, the high cost of indium as a raw material and process restraints make this system less attractive for low-cost PV applications [1]. Furthermore, ITO introduces interfacial diffusion problems when used in low-cost organic PV technology. In efforts to stray away from ITO the present work concentrates on titanium doped tungsten oxide (W-Ti-O) thin films grown by co-sputter deposition. The tactic of the research is to fabricate WO_3 thin films by adding Ti for TCO usage. Ti-doping will be incorporated in order to improve the conductivity of WO_3 leading to a suitable photocurrent. Also, the W-Ti-O system will optimize the transparency in order to replace the utilization of ITO. The growth conditions effect on the optical properties, crystal structure, film thickness, grain size and microstructure is essential to understanding the electrical properties and device performance. The reminder of this chapter is focused to present an overview of the literature efforts and merits of the W-Ti-O system.

1.1 Thin Films

The solar cells lie in front of a PV device covered with a thin layer of film that attracts the radiation from the sun. These devices are commonly known as a thin film and are made from semiconductor material. Thin films have become a thriving material due to their ability to convert sunlight to electrical power through the photovoltaic effect. Thin films are fabricated through a chemical vapor deposition (CVD) or physical vapor deposition (PVD) method and are usually no more than a few micrometers thick. Thin film photovoltaic cells are a renewable form of energy that is efficient and cost effective. The thinness of these thin film PV cells is a defining characteristic. Since these thin films are efficient there is no need for thickness. Adding a metal coating becomes essential to thin films because it enables the physical or optical properties to be altered.

1.2 Transparent Conducting Oxides (TCO) and Photovoltaics (PV)

Photovoltaic refers to the conversion of light into electricity using electronic devices. The assembly of a basic PV device can be seen in Figure 2. PV devices have gained interest because the devices are cost effective and since there are no moving parts present little maintenance is required. In addition, they produce electricity without noise or air pollution which is environmental and green friendly.

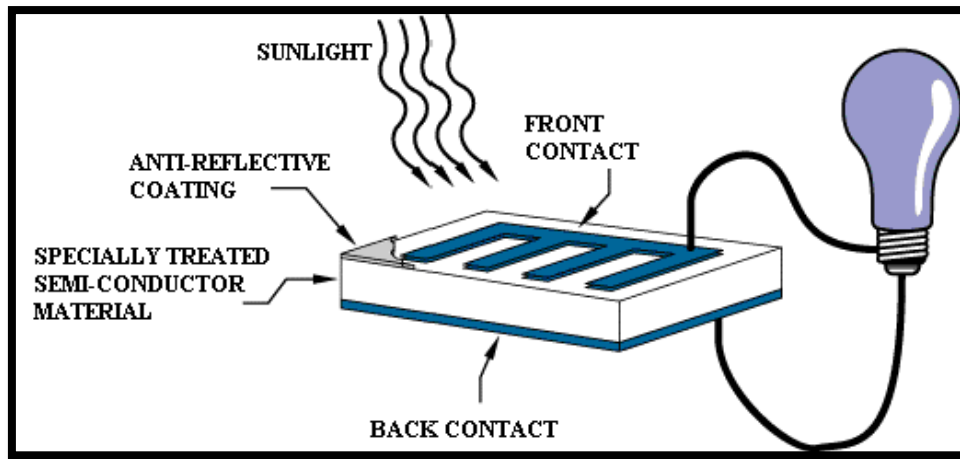


Figure 2. Assembly of a basic photovoltaic device.

The vast amount of PV technologies employs transparent conducting oxides as an integral part of the basic device structure [1]. The first TCO was reported in 1907 by Baedeker who used a primitive vapor deposition system to deposit thin-film CdO that was both optically transparent and electrically conductive [2]. The assembly of a TCO is a challenge since the material must be transparent and conductive simultaneously. Generally, for a material to be transparent across the visible spectrum, its bandgap must be greater than 3 eV to enable transmission up to the near UV (0.4 μm) wavelength [1]. On the other hand, conductive materials have lower energy band gaps. The needs and requirements of new PV technologies extend beyond the conventional TCO characteristics of transparency and conductivity. There is an increase desire to employ TCO layers as diffusion barriers, to control the contact work function and to have the TCO also act as a light trap [1].

Currently, the common TCO being used for display applications is indium tin oxide (ITO) due to its physical and chemical properties [1,3]. ITO is used as a charge carrier collecting electrode. However, there is a high demand to develop an indium free material due to indium's scarcity in the world and high cost [1-5]. In order to replace ITO a material must

compete with its properties listed in Table 1. A promising alternative to ITO thin films are tungsten oxide (WO_3) thin film because of their electrochromic properties.

Table 1. Common ITO properties.

Resistivity ($\Omega \text{ cm}$)	10^{-4}
Band gap (eV)	3.7
Index of refraction	2.0

1.3 Tungsten Oxide (WO_3)

Tungsten oxide (WO_3) is a fascinating material that has gained a massive amount of attention due to its coloration effects making it a “chromogenic” material [7-13]. Tungsten oxides are semiconductor metal oxide materials that have band gaps in the range of 2.6-3.0 eV [22]. WO_3 is used in a wide range of applications to include flat-panel displays, smart windows, electrochemical industry, selective catalysis, energy-efficient architecture of buildings and automobiles and chemical and mechanical sensors [13-26]. Most recently this material has been considered available to use in photoelectrochemical cells by water-splitting due to the associated photocatalytic properties [27-30]. In the field of water splitting, mainly n-type metal oxides like TiO_2 , Fe_2O_3 and WO_3 have attracted most of the attention due to their low cost, ease of preparation and high stability in aqueous solution under oxygen evolving conditions in a reasonably wide range of pH [30-33].

The ideal WO_3 cubic structure follows the ReO_3 -type perovskite structure shown in Figure 3 [56-58]. The tungsten ions occupy the corner sites while the oxygen ions bisect the unit cell edges. Since each tungsten ion is surrounded by six oxygen ions, the structure consists of WO_6 -octahedra arranged in various configurations. Figure 4 illustrates the octahedral layers stacked in arrangements which are held together by weak van der Waals forces. As the layers are stacked along the z-axis tunnels are formed. The tunneling allows ion intercalation or ionic transport which is a mechanism for electrochromic materials [56-58].

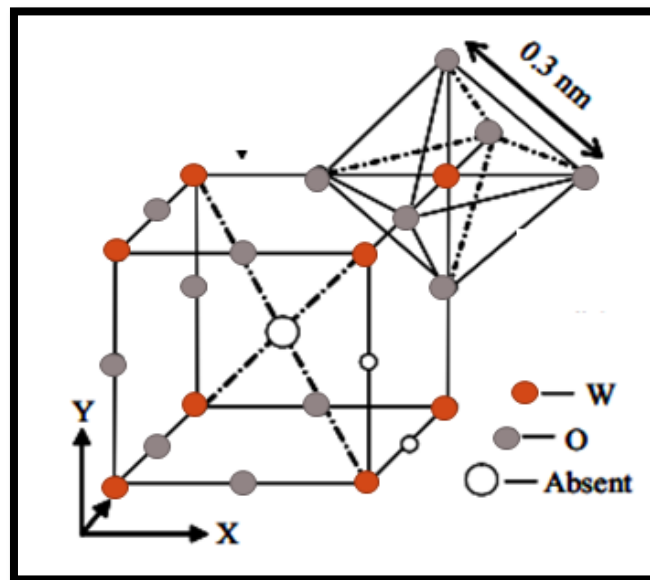


Figure 3. ReO_3 -type Perovskite WO_3 Structure [56-58].

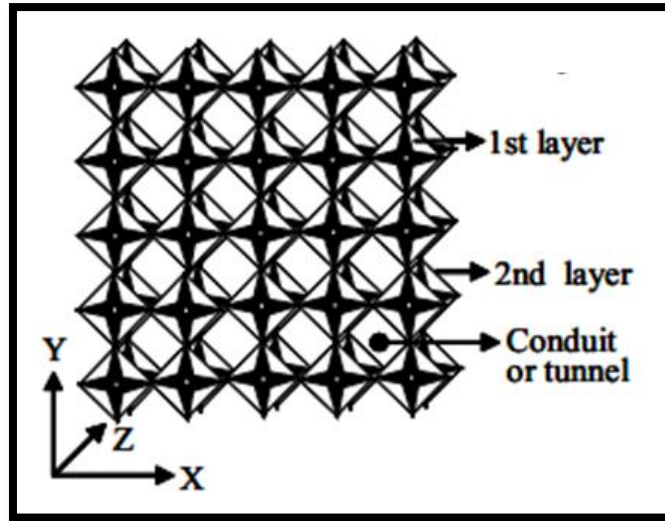


Figure 4. WO₃ layers create tunneling for ion transport [56-58].

The technique used to fabricate the films plays a significant role in the microstructure and electrical properties of the film. These materials are required to manifest the following parameters to be a fine sensor performing TCO material: a transmittance above 80%, a resistivity below $10^{-3} \Omega\text{cm}$, charge carrier concentration above 10^{20} cm^{-3} and an energy band gap of $\sim 3\text{eV}$ [1-3, 31]. Achievement of the lowest resistivity is of practical significance in the respect that it provides some flexibility in selecting the film thickness in order to achieve high optical transmission [3]. However, WO₃ is a complex material due to its phase transformation sequence as a function of temperature and pressure making it challenging to meet the TCO parameter requirements [35-39]. The following phase transformations occur due to atomic displacements, rotation of the WO₆-octahedra and the deposition conditions. Bulk WO₃ crystallizes in a triclinic structure and at higher temperatures it experiences the following phase transformations (Figure 5): triclinic ($\sim 30^\circ\text{C}$) \rightarrow monoclinic (330°C) \rightarrow orthorhombic (740°C) \rightarrow tetragonal [35-40].

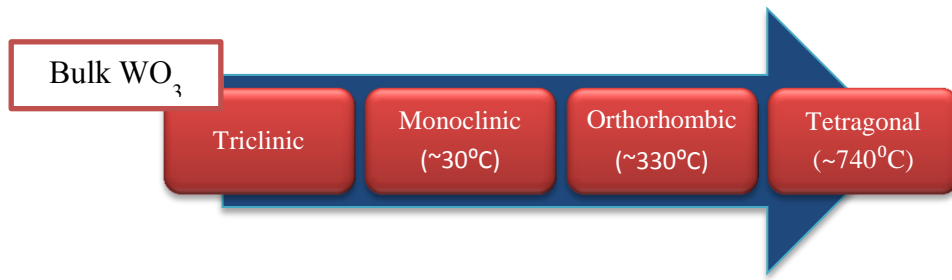


Figure 5. WO₃ polymorphism

Previously, Ramana's research group produced high quality WO₃ thin films under varying growth conditions. The results of the study showed a decrease in the strain energy with an increase in the substrate temperature (T_s) and an average grain size from 12-62nm (100-500°C) [20]. Most importantly, WO₃ crystallizes at 200 °C shown in Figure 6 [20]. In addition, a correlation was found between the T_s , transmittance (%T) and energy band gap (E_g); as T_s increase the %T decreases and the E_g decreases from 3.25 to 2.92 eV (room temperature (RT)-500°C) [43]. Tungsten oxide is a promising material for PV applications due to its electrical conductivity and excellent sensitivity and selectivity [6,46-49].

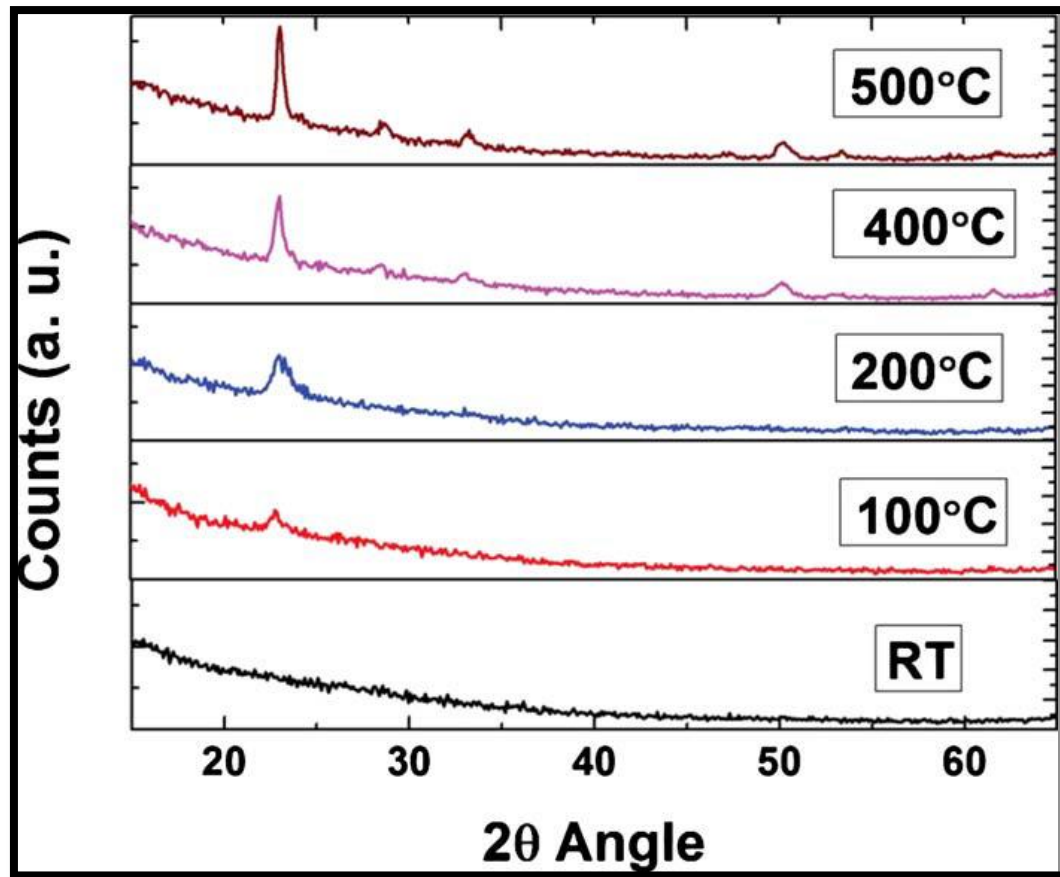


Figure 6. XRD pattern of WO₃ films grown at various temperatures [20]

1.4 Titanium Doping

The leading criterion when searching for a novel material would be starting with a metal-oxide semiconductor that has already publicized great characteristics, such as WO₃ in this case, and adding another properly chosen metal. A detailed study of the microstructural, electrical and optical properties is essentials when searching for new materials. To become conducting, the oxide must be doped to degeneracy by increasing the free carrier density enough to move the Fermi level into the conduction band [1]. Therefore, by doping WO₃ with titanium (Ti) the photochemical and electric properties can be altered, potentially making it an adequate transparent conducting oxide (TCO) for photovoltaic devices. Titanium, as an element, is a transition metal, exhibits relatively high transmittance and excellent resistance

to corrosion. Most importantly Ti is the ninth most abundant element in Earth's crust making it 25 times cheaper than indium.

Investigations have already proven W-Ti alloy films to exhibit low electrical resistance, thermal stability, oxidation resistance, inertness, good adhesion toward metal contact and the substrate and high refractive index [41-43]. Therefore, W-Ti-O films will possibly modify the microstructure and properties of the material. In a prior study conducted by Kalidindi *et. al.* it was found that Ti inhibits the crystallization, increases the temperature for crystal growth, and inhibits the grain growth compared to pure WO₃ films [16]. Moreover, an investigation was done on W_{0.95}Ti_{0.05}O₃ (W-Ti-O) films that were grown by alloy target sputtering in Ramana's group and demonstrate interesting results. In Figure 7 it is evident that the amorphous-to-crystalline transition temperature is 300 °C for W-Ti-O films which is higher than that of pure WO₃ films (200 °C) [14].

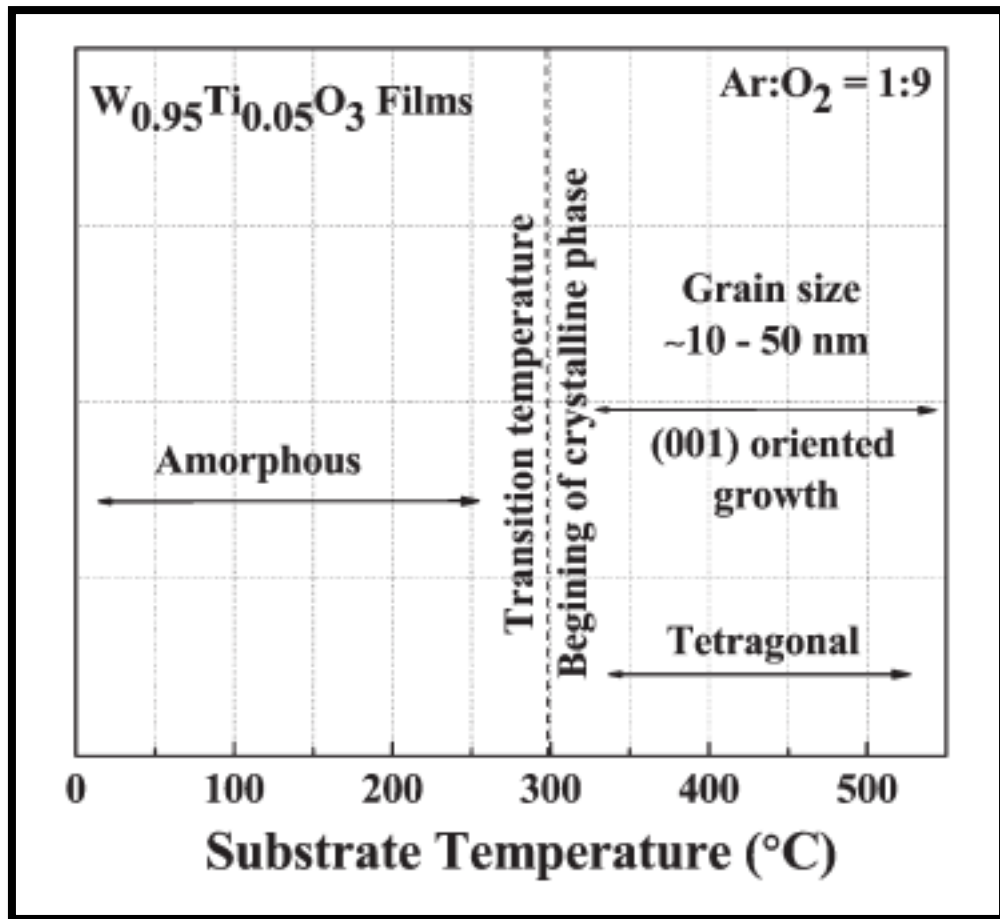


Figure 7. Phase diagram summarizing the microstructure evolution of $W_{0.95}Ti_{0.05}O_3$ films as a function of temperature [14].

Additionally, with an increase in T_s the average crystallite size increases along with the conductivity, graphed in Figure 8 [13-14]. Furthermore, a study was done to understand WO_3 films by varying the O_2 content and the results show that as O_2 content increases the film density increases, the film thickness decreases, the particle size decreases, the deposition rate decreases and the growth rate also decreases. Although, there has been an abundance of research done on WO_3 and its properties through different fabrication methods, the co-sputter method has yet to be investigated. The co-sputter method consist of two metal targets, in this case Ti and W, under a controlled amount of power to obtain the desired amount of Ti and WO_3 deposited on the substrate.

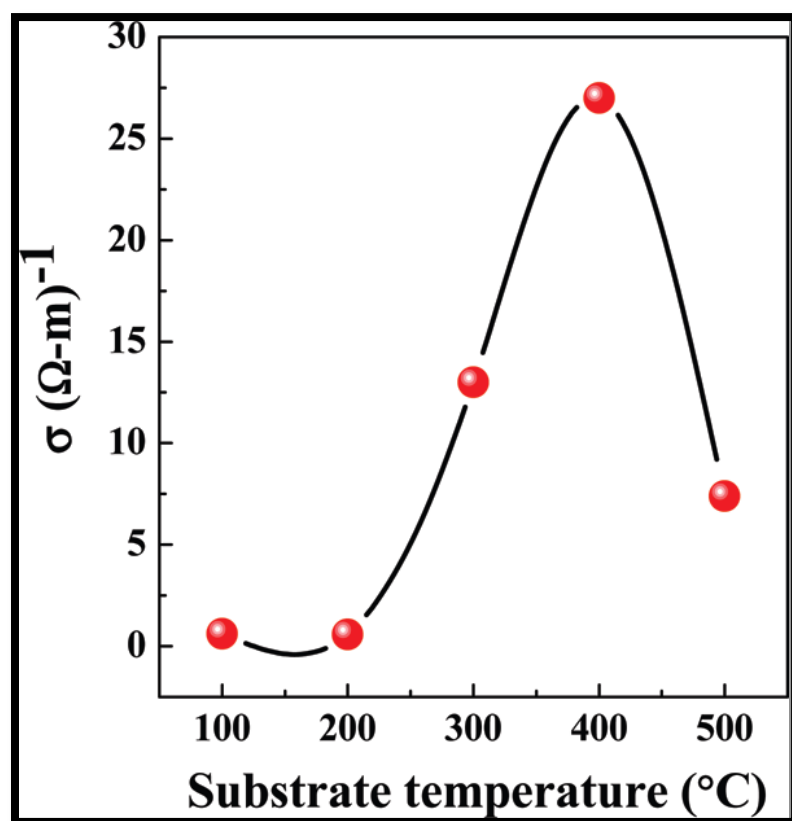


Figure 8. Variation in electrical conductivity of $\text{W}_{0.95}\text{Ti}_{0.05}\text{O}_3$ films with substrate temperature [14].

Chapter 2: Experimental Methods

3.1 Physical Vapor Deposition and Sputter Deposition

Physical vapor deposition (PVD) is an important technique when it comes to thin film fabrication. The common PVD methods used is sputtering and the evaporative process. PVD processing allows a chemical to become a vapor and go straight onto the glass substrate as a molecule without decomposing; no chemical reaction occurs. PVD is desired since it is a thickness and deposition rate controlled method. Sputtering occurs when the desired film materials is released from a source material (metal target) by a high energy bombardment. These ejected molecules or atoms travel to the substrate where they condense or deposit as a thin film. Correspondingly, the PVD sputtering technique is a low pressure plasma environment while having a controlled uniformity due to the magnetron. Fewer contaminants are present in the sputtering method and in comparison to the evaporative method, sputtering develops better adhesion between the substrate and deposited film. Figure 9 illustrates the co-sputter technique utilizing a Ti and W metal target. The co-sputter method occurs by simultaneously sputtering the two targets in order to obtain a homogenous deposition of mixed compositions.

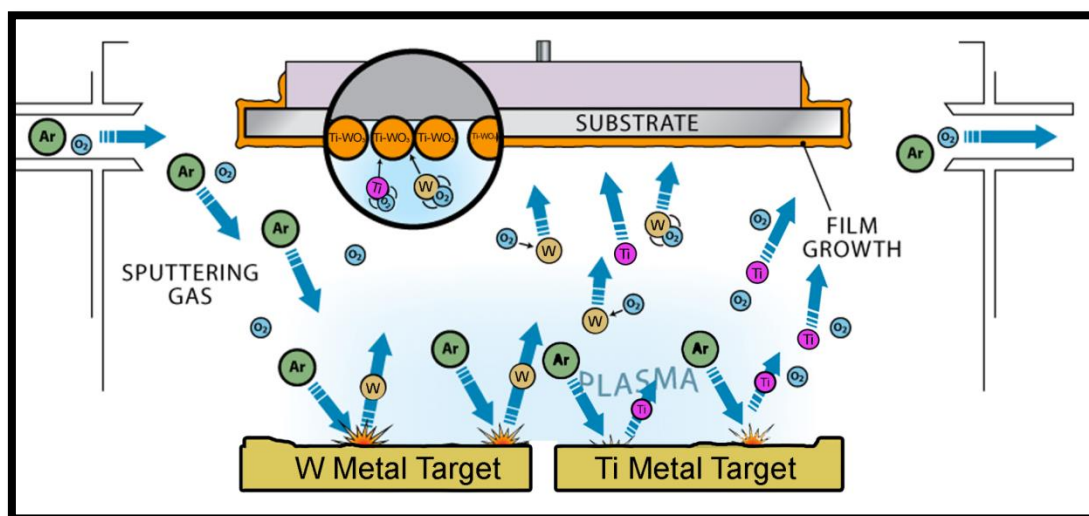


Figure 9. Co-sputter deposition using Ti and W metal targets.

3.1.1 Fabrication

W-Ti-O films were deposited on Si (100) wafers and optical grade quartz by radio-frequency (RF) (13.56 MHz) magnetron sputtering. The Si (100) substrates were cleaned by RCA cleaning. Prior to introducing the substrates into the vacuum chamber all substrates were thoroughly cleaned and dried in nitrogen, which was initially evacuated to a base pressure of $\sim 10^{-6}$. Tungsten (W) and Titanium (Ti) metal targets (Plasmaterials Inc.) of 2 in. diameter and 99.95% purity was employed for reactive sputtering. The targets were placed on a 2 in. sputter gun, which is placed at a distance of 8 cm from the substrate. A sputtering power of 40W was initially applied to the target. In order to ignite the plasma, high purity argon (Ar) was introduced. Once the plasma was ignited, the sputtering power was increased to the desired or set values for W and Ti targets, respectively. A sputtering power of 100W was maintained constant for the W target while the applied sputtering power to the Ti target varied from 50 to 100W to vary the concentration of Ti atoms in the film. The flow of Ar and O₂ was controlled using as MKS mass flow meters. In order to ensure the targets were clean before each deposition, the targets were pre-sputtered for 10 minutes using Ar while the shutter above the gun remained closed. The depositions were carried out from 30 min to an hour. The samples were deposited at substrate temperatures (T_s) from room temperature (RT) to 500 °C. The substrates were heated by halogen lamps and the desired temperature was controlled by Athena X25 controller. The following tables represent the grown films at constant flow rates of O₂ at 10 sccm and Ar at 30 sccm.

Table 2. Effect of temperature -WO₃ grown films.

Temperature	Sample- Sputtering Power (watts)	Duration
RT	W-100W Ti-50W	30min
200°C	W-100W Ti-50W	30min
300°C	W-100W Ti-50W	30min
400°C	W-100W Ti-50W	30min
500°C	W-100W Ti-50W	30min

Table 3. Effect of increasing Ti sputtering power - WO₃ grown films.

Temperature	Sample	Duration
400 & 500°C	W-100W Ti-50W	1hr
400 & 500°C	W-100W Ti-70W	1hr
400 & 500°C	W-100W Ti-100W	1hr

3.2 Characterization

3.2.1 X-Ray Diffraction

The crystal structure of the W-Ti-O films deposited on the silicon wafers was determined using X-ray diffraction (XRD) which is also known as Bragg diffraction. Figure 10 illustrates the Bruker D8 Advance X-ray diffractometer which was used at UTEP for this research.

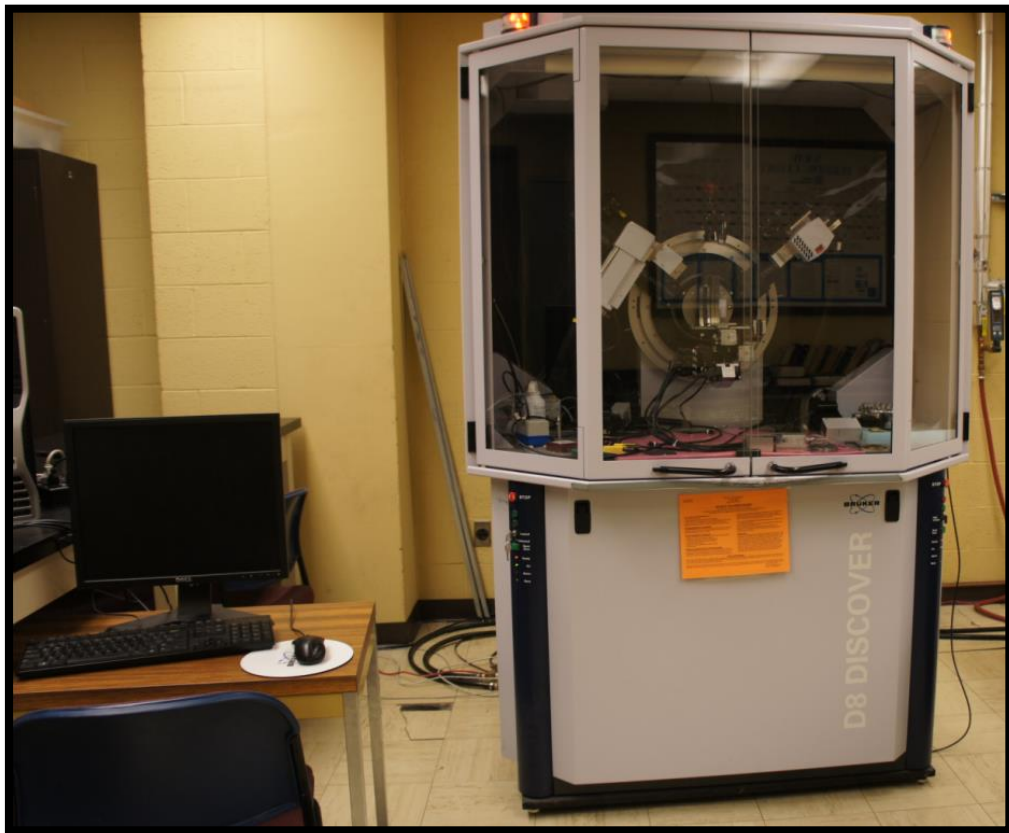


Figure 10. Bruker D8 Advance X-ray diffractometer

X-ray diffraction is a phenomenon where the atomic planes of a crystal cause an incident beam of X-rays to interfere with one another as they leave the crystal. The XRD operates by the scattering of X-rays, by a crystal atom, which in return produces a diffraction that

yields information about the structure of the crystal (Figure 11). The diffracted x-rays beam provides several information about the film crystallography and inter-planar atomic distance “d” between the two planes of film. A given wavelength diffraction can only occur at a certain angle and d- spacing. Braggs Law then comes into play which is as follows:

$$\lambda = 2d\sin\theta$$

Where λ =wavelength of X-ray, d=inter planar distance and θ = Bragg’s angle.

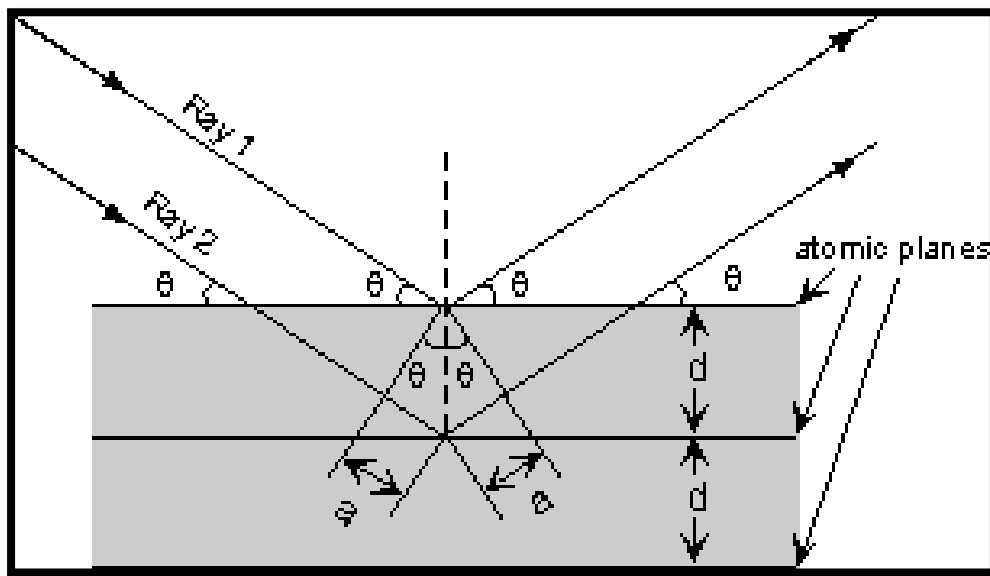


Figure 11. Bragg’s law through X-ray diffraction.

All the measurements were made *ex situ* as a function of T_s and T_i sputtering power. XRD patterns were recorded using a Cu $K\alpha$ radiation ($\lambda=1.54056 \text{ \AA}$) at room temperature. Calculations of the coherently diffracting domain size (d_{hkl}) were made using the Scherrer’s equation using the integral width of the diffraction lines after eliminating the background. The Scherrer equation is [45]:

$$d_{hkl} = \frac{0.9\lambda}{\beta \cos \theta}$$

where d_{hkl} is the size, λ is the wavelength of the incident X-radiation, β is the width of the most intense peak at half of its intensity, and θ is the angle of the peak.

3.2.2 Scanning Electron Microscopy

Surface imaging analysis was performed using a high performance and ultrahigh resolution scanning electron microscope (Hitachi S-4800) shown in Figure 12. An electron beam incident on the sample surface ejects the weakly bonded electrons called secondary electrons (SE). These electrons have low energy and can be detected by the detector to produce an SEM image of the sample surface up to 1 micrometer in depth. The low energy SE's can be affected by the electromagnetic field. To avoid charge build up on the sample surface, the sample must be properly attached to a conductive copper tape strip or a coating of graphite.



Figure 12. Hitachi S-4800 Scanning Electron Microscope (SEM)

To produce the beam, electrons are thermionically emitted from a cathode tungsten filament and drawn to an anode. The electron beam energy can be employed in a range from 0.5 KeV to 40 KeV. Two condenser lenses in the vacuum chamber are used to focus the

beam to a surface area of 1 nm to 5 nm in diameter. The path of the beam on the sample surface follows a raster scan pattern. Sweeping from left to right, it blanks as it rapidly moves back to the left position and scans the next line downwards. When the primary electrons from the beam hit the sample, its energy is high. The high energy beam loses its energy by random scattering and absorption. Due to the low energy of the excited secondary electrons, they can be detected by the SE detector and produce the SEM image.

3.3 Optical Analyses

The optical properties of W-Ti-O films grown on quartz substrates were evaluated using spectrophotometry measurements employing Cary 5000 UV-vis-NIR double-beam spectrophotometer. Cary 5000 UV-VIS-NIR optical spectrometer (Fig. 13) is used for optical absorption spectroscopy in the wavelength range of 200-2000 nm. The optical characterization is usually performed on highly transparent and semi-transparent thin films deposited on transparent substrates such as quartz.

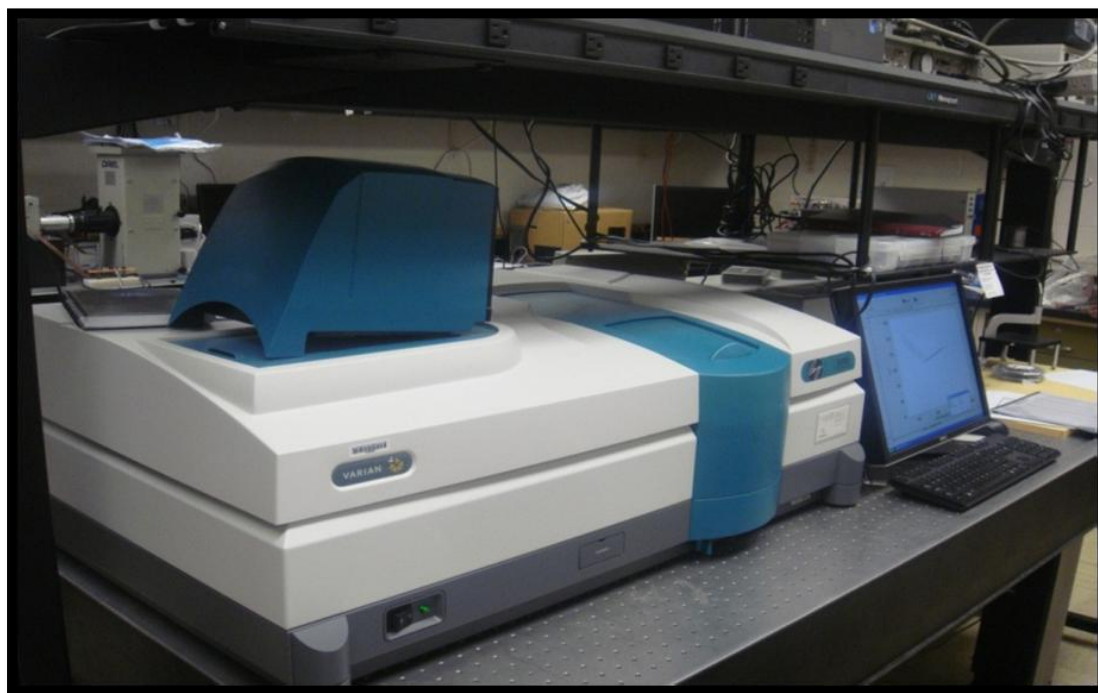


Figure 13. Cary 5000 UV-VIS-NIR optical spectrometer

3.3.1 Energy Band Gap (E_g)

The region of an atom in a solid material represented by an energy range in the electronic band structure where no electrons can exist is called the band gap or energy gap (E_g) [52]. The measurement of the band gap of materials is important in the semiconductor, nanomaterial and solar industries. The term “band gap” refers to the energy difference between the top of the valence band to the bottom of the conduction band (see Figure14); electrons are able to jump from one band to another [53]. In order for an electron to jump from a valence band to a conduction band, it requires a specific minimum amount of energy for the transition, the band gap energy. The bandgap is important as it determines the portion of the solar spectrum a photovoltaic cell absorbs [53].

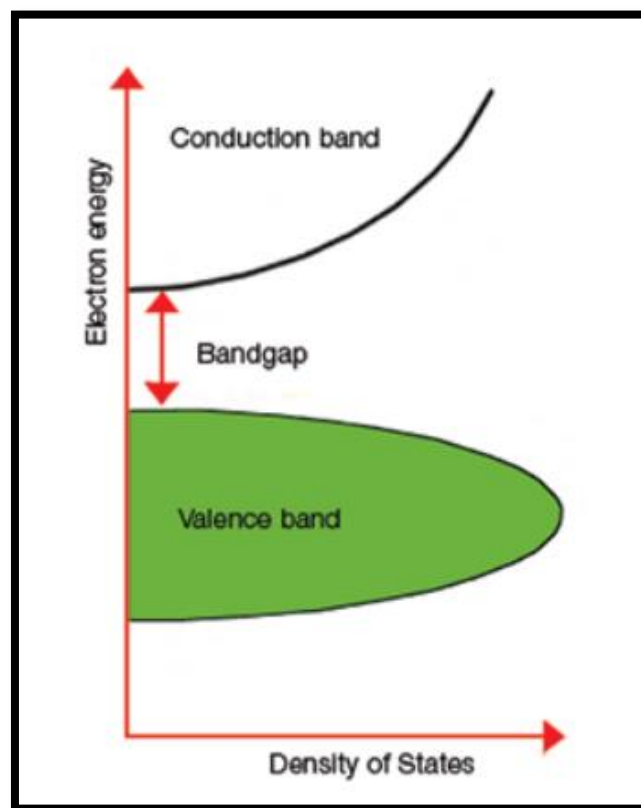


Figure 14. Explanation of band gap [53]

In an indirect band gap semiconductor, the maximum energy of the valence band has a different momentum value as compared to the minimum energy of the conduction band [54]. This process is slower and requires more momentum in order to jump from the valence band to the conduction band, since it requires a photon, an electron and the intervention of a phonon (see Figure 15).

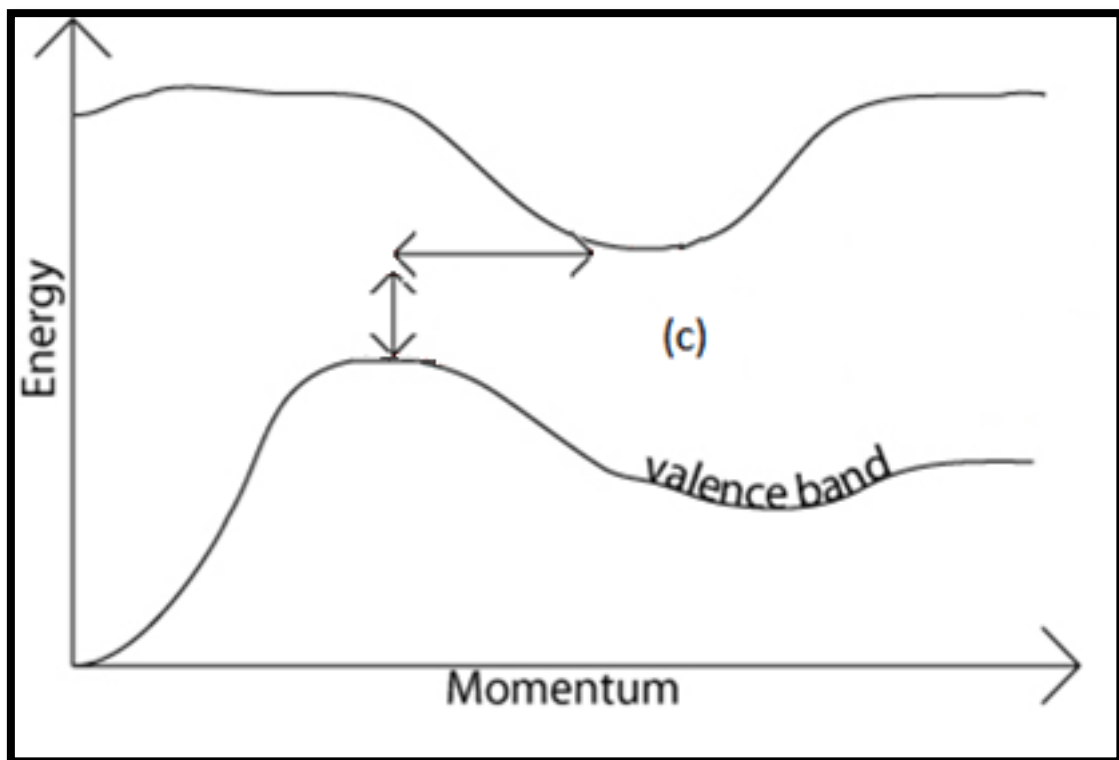


Figure 15. Indirect band gap [54].

For WO_3 with an indirect band gap, in the E_g region (high absorption) or above the fundamental absorption edge, the absorption follows a power law of the form [4,8,16,43]

$$(\alpha h\nu) = B(h\nu - E_g)^2$$

Where $h\nu$ is the energy of the incident photon, B is the absorption edge width parameter, α is the absorption coefficient, and E_g is the band gap. The absorption coefficient, α , is calculated using the relation [16,43,55]

$$\alpha = \frac{1}{t} \ln \left[\frac{T}{(1-R)^2} \right]$$

where T is transmittance, R is reflectance and t is the film thickness.

Chapter 3: Results and Discussions

3.1 XRD Results

Crystal structure analysis of W-Ti-O films was performed using X-ray diffraction (XRD). The XRD patterns obtained for W-Ti-O films are shown in Figure 16, where the results shown as a function of the substrate temperature (T_s). Additionally, Figure 17 shows the XRD patterns as a function of Ti-target sputtering power. The XRD curves at RT did not illustrate any peaks indicating an amorphous ($a\text{-WO}_3$) nature. Crystallization begins at temperatures between 200 °C- 400 °C where they transform to monoclinic WO_3 ($m\text{-WO}_3$). At a substrate temperature of 500 °C a structural transformation occurs leading to the tetragonal phase ($t\text{-WO}_3$). The amorphous state occurs because of the short relaxation period where deposited flux do not exhibit enough kinetic energy on the substrate. On the other hand, the crystalline state occurs due to thermal energy provided at higher temperature and deposited flux undergo structural re-arrangement.

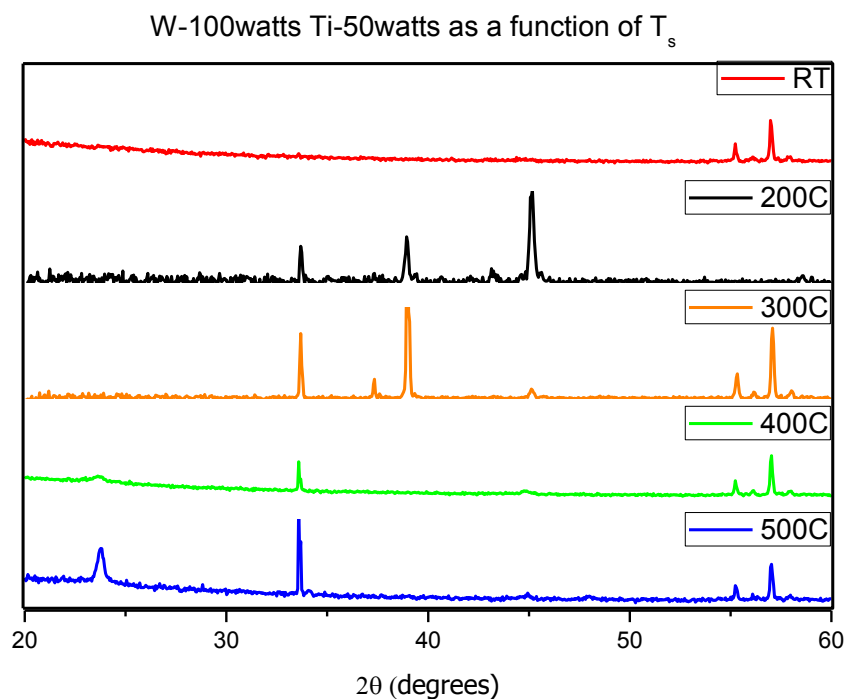


Figure 17. XRD patterns of co-sputtered W-Ti-O films grown at various temperatures.

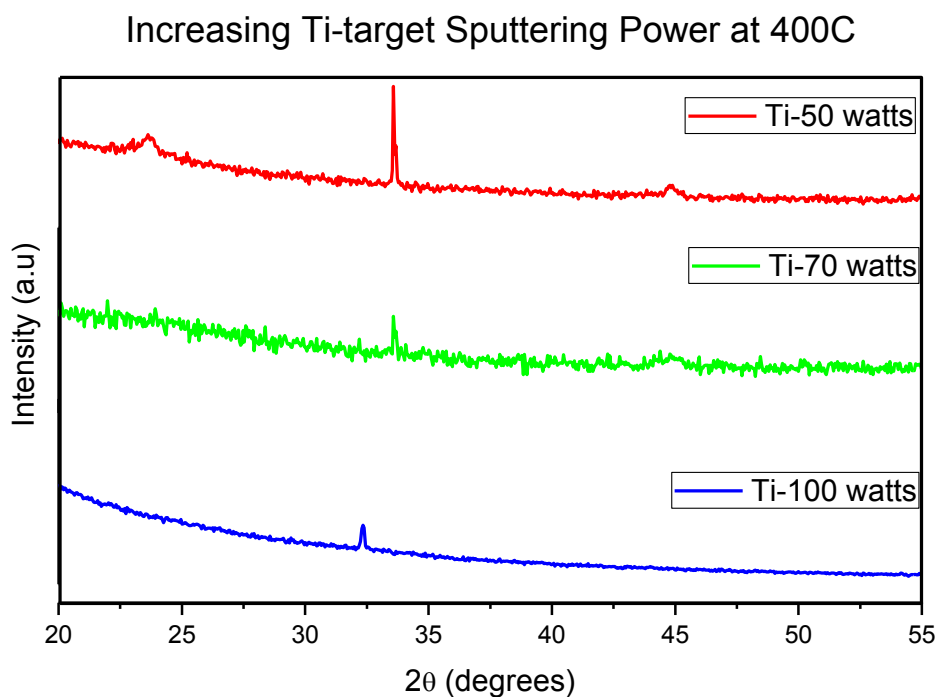


Figure 17. XRD patterns of W-Ti-O co-sputtered films with increasing Ti sputtering power.

The most intense peak at hand is at $2\theta=33.66^\circ$ which is indicative of the (220) diffraction plane. Ti is not present in the XRD patterns since it is in solid solution in the tungsten matrix. Results of previous investigations on pure WO_3 show the film crystallization at $T_s=100\text{-}200^\circ\text{C}$.⁴⁰ Therefore, it is evident that Ti does in fact prevent crystallization of WO_3 and raises its crystallization temperature. Computations of the Scherrer equation resulted in a grain size from 75-135 nm with an increase in substrate temperature. Larger grain size leads to better electric conductivity due to the less grain boundaries existing in the film resulting in reduced density of trapped free charge carriers. Therefore, the free carrier concentration is expected to increase with increasing substrate temperature.

4.2 SEM Results

The SEM images characterizing the surface morphology of the films are shown in Figure 18 and 19. The SEM images are in agreement with the XRD results for a- WO_3 since there are no features that can be seen at RT, even at high magnifications. If the temperature is low such that the period of the atomic jump process of adatoms on the substrate surface is very large, the condensed species may stay stuck to the regions where they are landing thus leading to an amorphous nature W-Ti-O films. The adatom mobility on the surface increases with increasing temperature [41]. A few small spherical particles can be seen in Figure 13 at 400°C which indicates the growth of nanocrystalline W-Ti-O films. At a substrate temperature of 500°C it can clearly be seen that a granular microstructure exist. By doping WO_3 with Ti it again can be concluded that Ti increases the temperature for crystal growth. Unfortunately, mapping through EDS could not be done due to the low voltage requirements.

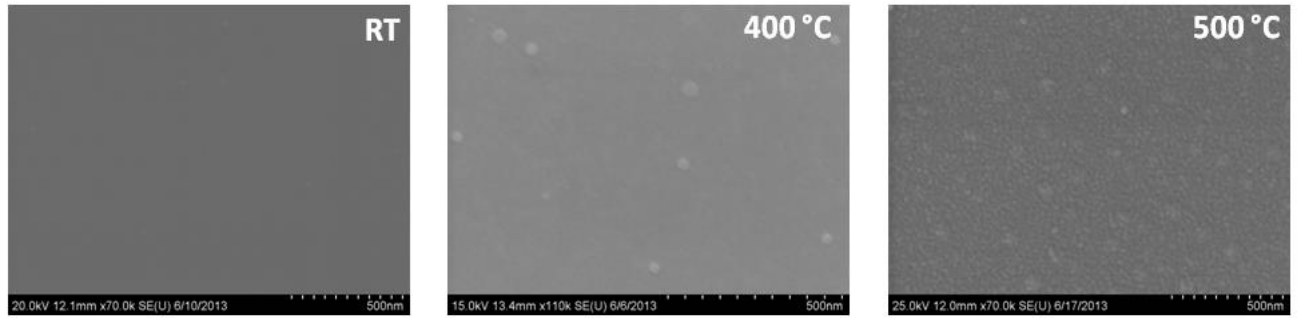


Figure 18. The high-resolution SEM images of W-Ti-O films with a sputtering power of Ti-target at 50W as a function of substrate temperature

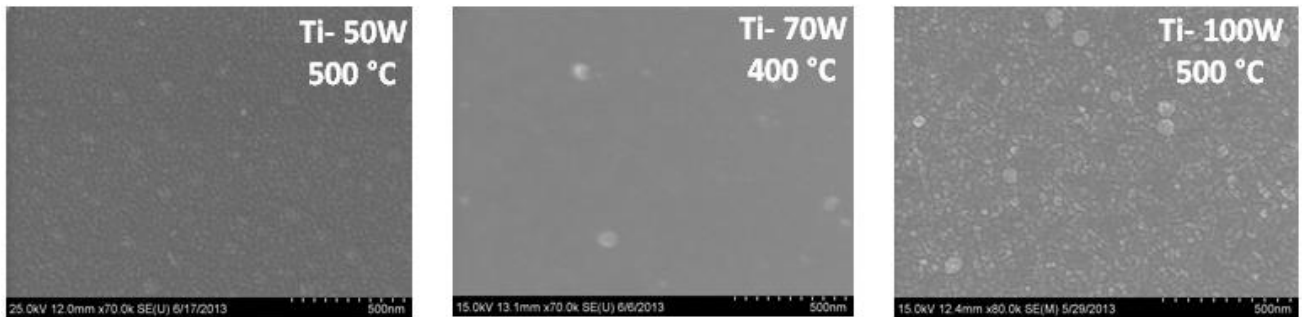


Figure 19. The high-resolution SEM images of W-Ti-O films as a function of Ti-target sputtering power.

4.3 Optical Results

Figure 20 illustrates the spectral transmission characteristics of W-Ti-O films as a function of substrate temperature. The spectral transmission curves reveal that the W-Ti-O films in general show a high transparency in the spectral region except where the incident radiation is absorbed across the band gap (E_g) and the dips noticed in the spectra are due to interference. This observation indicates the high-quality and transparent nature of W-Ti-O films. In Figure 21 a significant shift in the transmittance peak is noted for the grown W-Ti-O films as a function of Ti sputtering power indicating a change in the band gap of the materials fabricated due to the amount of Ti present.

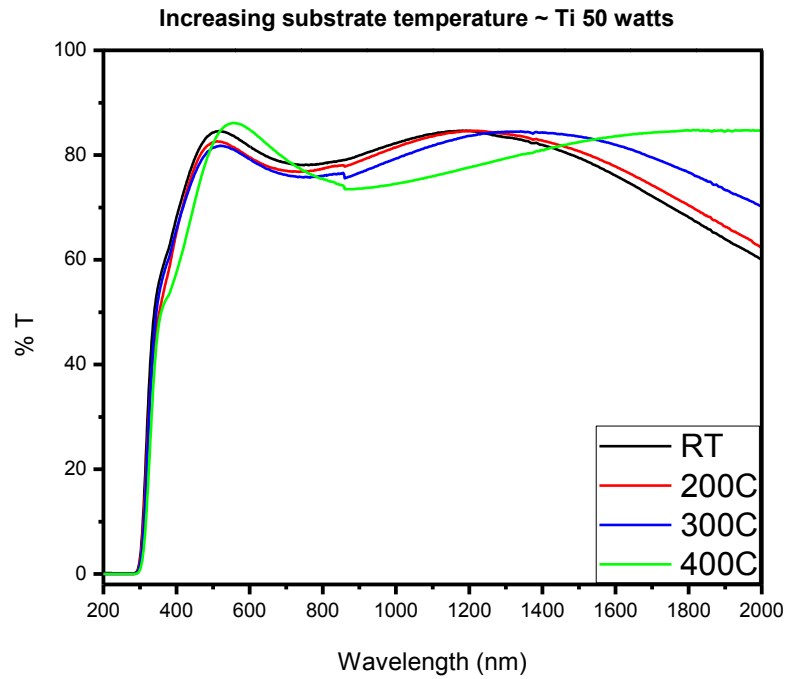


Figure 20. Optical transmittance spectra of W-Ti-O films with a sputtering power of Ti-target at 50W as a function of substrate temperature

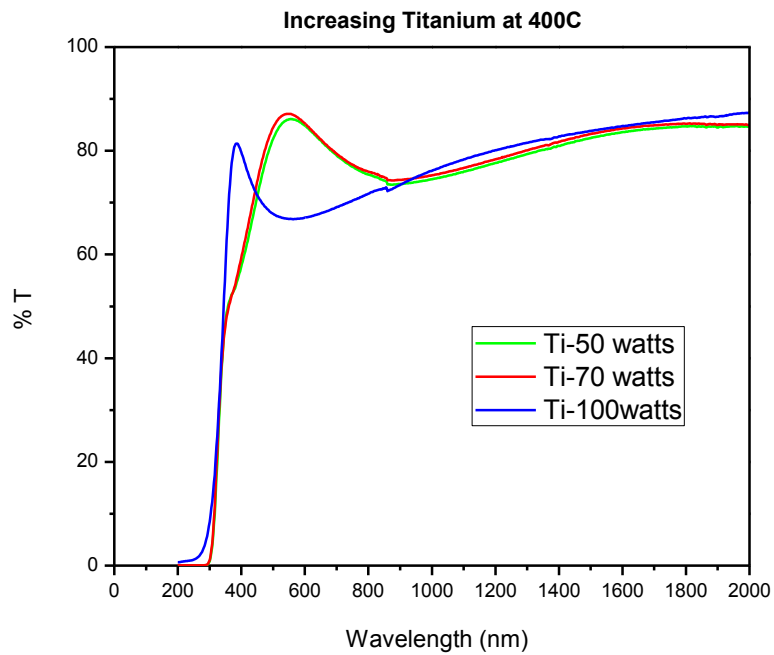


Figure 21. Optical transmittance spectra of W-Ti-O films as a function of Ti-target sputtering power.

The amount of light retained by the material is known as the absorption coefficient. A linear least-square fit on the straight-line character of the absorption edge is incorporated. This slope determines how fast the material starts absorbing the light, in return yields the energy band gap of the material. The absorption spectra of W-Ti-O at 50 watts sputtering power as a function of substrate temperature is represented in Figure 22. In order to determine the effect of Ti on the absorption the data was analyzed shown in Figure 23. It is evident that the substrate temperature influences the absorption across the band gap and with increasing Ti the absorption edge shifts to lower spectral region indicating an increase in the absorption edge.

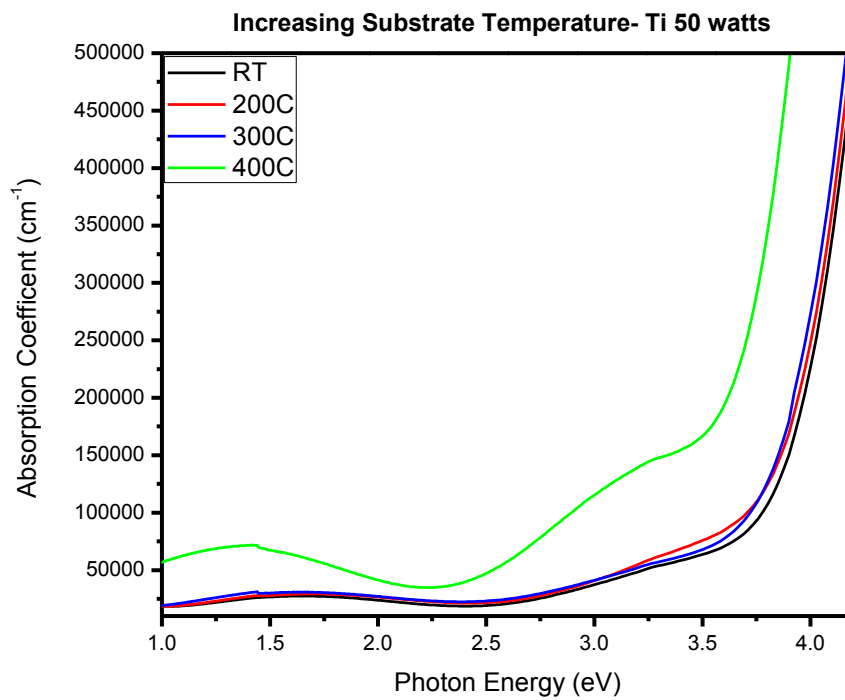


Figure 22. Absorption data of W-Ti-O with a sputtering power of Ti-target at 50W as a function of substrate temperature.

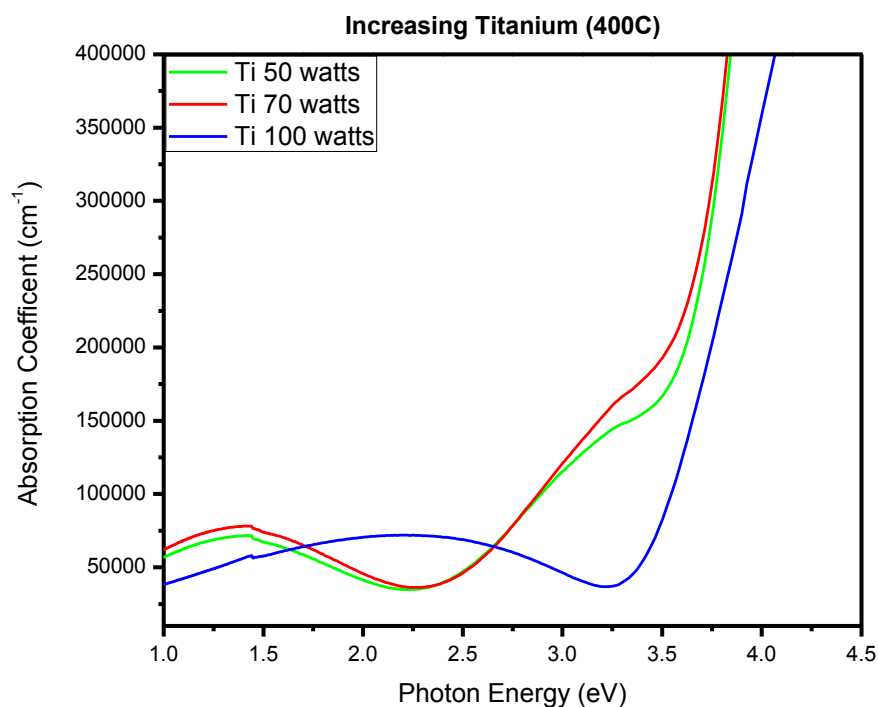


Figure 23. Absorption data of W-Ti-O as a function of Ti-target sputtering power.

The E_g values determined by extrapolating the linear region (Figure 24) of the plot to $h\nu=0$, increases from 2.9- 3.6 eV with increasing T_s and increases from 2.8-3.3 eV with an increase in Ti. The decrement in the band gap with increasing substrate temperature is due to the crystallization of the films.

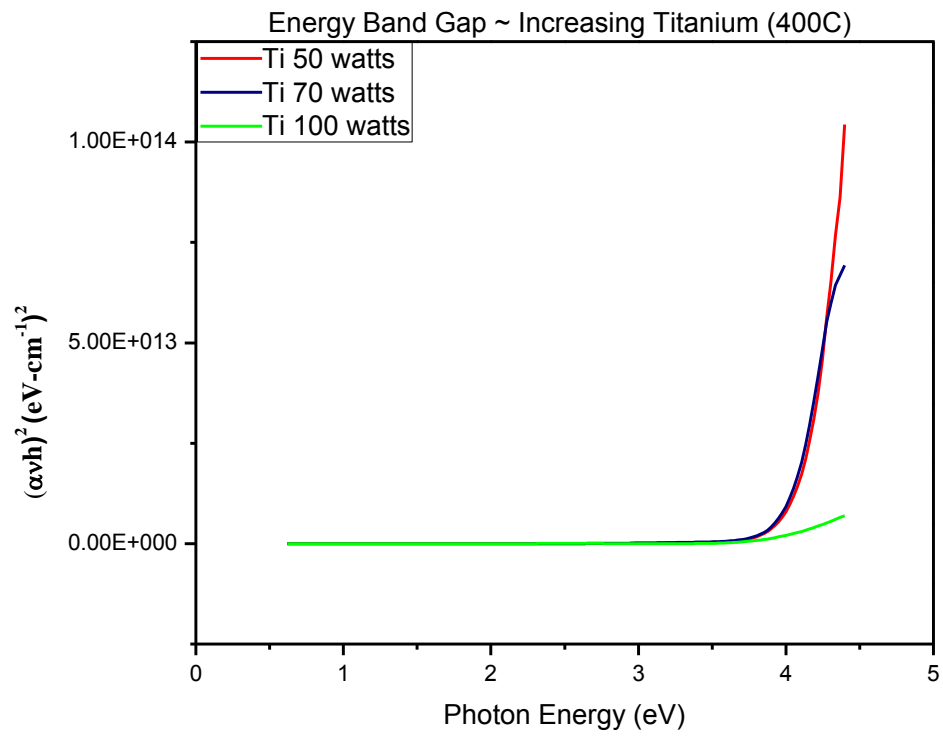


Figure 24. $(\alpha h\nu)^{1/2}$ vs $h\nu$ plots for W-Ti-O films grown at various Ti-target sputtering power. Extrapolating the linear region of the plot to $h\nu=0$ provides the band gap value.

Chapter 4: Conclusions

Titanium doped WO_3 thin films were fabricated using co-sputter deposition under varying deposition temperatures (RT-500 °C) and Ti- sputtering powers (50 watts-100 watts) in order to analyze the effect of temperature and titanium. The XRD results indicate that the W-Ti-O films grown at RT are amorphous, monoclinic at 200°C and transform to tetragonal at 500°C. Ti peaks are not evident in the XRD patterns since it is in solid solution in the W matrix. The increase in temperate and the addition of Ti inhibits the crystallization of WO_3 . The SEM imaging analyses agree with the XRD results indication the crystallization at 200°C. The spectral transmission curves show a high transparency. An increase in T_s influences the absorption across the band gap and with increasing Ti there is an increase in the absorption edge. The energy band gap decreases from 4.0 eV to 3.9 eV with an increase in substrate temperature due to the crystallization of the films and increases from 3.85 eV to 3.95 eV with an increase of Ti.

Chapter 5: Future Work

The parametric study and knowledge developed on W-Ti-O thin films and an understanding on the effect of Ti-doping on the surface morphology, crystal structure and optical data can be used for testing the PV device applications of these films. The addition of Ti proved to be a positive addition with the intent to replace indium tin oxide for the use of transparent conducting oxide materials in photovoltaic applications. Unfortunately, due to time restrictions, detailed electrical properties and efficiency of the W-Ti-O films is not tested. The future work could focus on these aspects along with computational work to evaluate the performance of these candidate materials.

References

1. E. Fortunato, D. Ginely, H. Hosono, and D. C. Paine, MRS Bull. **32**, 242-247 (2007).
2. T. Minami, Thin Solid Films, **516**, 1314-1321 (2008).
3. R. B. H. Tahar, T. Ban, T. Ohya, and Y. Takahashi, J. Appl. Phys. **83**, 5, 2631 (1997)
4. C. G. Granqvist, Handbook of Inorganic Electrochromic Materials; Elsevier: New York, (1995).
5. Y. Zhang, S. H. Lee, A. Mascarenhas, and S. K. Deb, Appl. Phys. Lett. **93**, 203508 (2008).
6. C. V. Ramana, S. Utsunomiya, R. C. Ewing, C. M. Julien, and U. Becker, J. Phys. Chem. B **110**, 10430-10435 (2006)
7. C. V. Berggren, J. C. Jonsson, and G. A. Niklasson, J. Appl. Phys. **102**, 083523 (2007).
8. S. Y. Lin, H. T. Chen, and J. Y. Lai, Thin Film Solids **518**, 1377 (2009).
9. D. Lu, J. Chen, H. J. Chen, J. Gong, S. Z. Deng, N. S. Xu, and Y. L. Liu, Appl. Phys. Letter **90**, 041919 (2007).
10. C. Bechinger, G. Oefinger, S. Herminghaus, and P. Leiderer, J. Appl. Phys. **74**, 4527 (1993).
11. K. Bange and T. Gambke, Adv. Mater. **1**, 10 (1990).
12. C. G. Granqvist, Solid State Mater. Sci. **16**, 291 (1990)
13. N. R. Kalidindi, K. Kamala Bharathi, and C. V. Ramana, Appl. Phys. Lett. **97**, 142107 (2010).
14. N. R. Kalodindi, F. S. Manciu, and C. V. Ramana, ACS Appli. Mater. Interfaces **3**, 863-868 (2011) .
15. A. Subrahmanyam, and A. Karuppasamy, Sol. Energy Mater. Sol. Cells **91**, 266-274 (2007).
16. A. Karuppasamy, and A. Subrahmanyam, Thin Solid Films **516**, 175-178 (2007).

17. M. Acosta, D. Gonzalez, and I. Riech, *Thin Solid Films* **517**, 5442-5445 (2009).
18. C. V. Ramana, and S. K. Gullapalli, *J. Mater. Res.* **25**, 12, 2401-2406 (2010).
19. D. Susanti, S. N. Haryo, H. Nisfu, E. P. Nugroho, H. Purwaningsih, G. E. Kusuma, and S. Shih, *J. Front. Chem. Sci. Eng.* **6**, 4, 371-380 (2012).
20. S. K. Gullapalli, R. S. Vemuri, F. S. Manciu, J. L. Enriguez, and C. V. Ramana, *J. Vac. Sci. Technol.* **A28**, 4, 824-828 (2010).
21. L. F. Zhu, J. C. She, J. Y. Luo, S. H. Deng, J. Chen, and N. S. Xu, *J. Phys. Chem. C.* **114**, 15504-15509 (2010).
22. L. Wang, S. E. Teleki, S. E. Pratsinis, and P. I. Gouma, *Chem. Mater.* **20**, 4794-4796 (2008).
23. A. Wolcott, T. R. Kuykendall, S. Chen, and J. Z. Zhang, *J. Phys. Chem. B* **110**, 25288-25296 (2006).
24. B. Marsen, E. L. Miller, D. Paluselli, and R. E. Rocheleau, *Int. J. Hydrogen Energy* **32**, 3110 (2007).
25. D. Paluselli, B. Marsen, E. L. Miller, and R. E. Rocheleau, *Electrochem. Solid-State Lett.* **8**, G 301 (2005).
26. Y. Sun, C. J. Murphy, K. R. Reyes-Gil, E. A. Reyes-Garcia, J. M. Thornton, N. A. Morris, and D. Raftery, *Int. J. Hydrogen Energy* **34**, 8476 (2009).
27. C. A. Bignozzi, S. Caramori, V. Cristino, R. Argazzi, L. Meda, and A. Tacca, *Chem. Soc. Rev.* **42**, 2228 (2013).
28. H. Wang, T. Lindgren, J. He, A. Hagfeldt and S.-E. Lindquist, *J. Phys. Chem. B*, **104**, 5686 (2000).
29. M. Santato, M. Odziemkowski, M. Ulmann and J. Augustynski, *J. Am. Chem. Soc.*, **123**, 10639 (2001).
30. M. Santato, M. Ulmann and J. Augustynski, *J. Phys. Chem. B*, **105**, 936 (2001).

31. T. Minami, *Semicond. Sci. Technol.* **20**, S35-S44 (2005).
32. W. Sahle, and M. J. Nygren, *Solid State Chem.* **48**, 154-160 (1983).
33. J. M. Berak, and M. J. Sienko, *Solid State Chem.* **2**, 109-133 (1970).
34. E. Salje, and K. Viswanathan, *Acta Crystallogr., Sect. A: Found.* **31**, 356-359 (1975).
35. T. Vogt, P. M. Woodward, and P. A. Hunter, *J. Solid State Chem.* **144**, 209 (1999).
36. E. Cazzanelli, C. Vinegoni, G. Mariotto, G. Kuzmin, and J. Purans, *J. Solid State Chem.* **143**, 24 (1999).
37. R. Chatten, A. Chadwick, A. and J. Lindan, *J. Phys. Chem. B*, **109**, 3146 (2005).
38. V. G. Glebovsky, V. Yu, Yaschak, V. V. Baranov, and E. L. Sackovich, *Thin Solid Films* **257**, 1-5 (1995).
39. V. Guidi, D. Boscarino, E. Comini, G. Faglia, M. Ferroni, C. Malagu, G. Martnelli, V. Rigato, and G. Sberveglieri, *Sens. Actuators B* **65**, 264 (2000).
40. N. Bundaleski, S. Petrovic, D. Perusko, J. Kovac, and A. Zalar, *Appl. Surf. Sci.* **254**, 6390-6394 (2008).
41. N. R. Kalidindi, F. S. Manciu, and C. V. Ramana, *ACS Appl. Mater. Interfaces* **3**, 863-868 (2011).
42. E. Washizu, A. Yamamoto, Y. Abe, M. Kawamura, and K. Sasaki, *Solid State Ionics* **165**, 175 (2003).
43. S. K. Gullapalli, R. S. Vemuri, and C. V. Ramana, *Appl. Phys. Lett.* **96**, 171903 (2010).
44. F. Z. Tepehan, F. E. Ghodsi, N. Ozer, and G. G. Tepehan, *Sol. Energy Mater. Sol. Cells* **59**, 265 (1999).
45. B. D. Cullity, and S. R. Stock, *Elements of X-Ray Diffraction*, 3rd ed; Prentice- Hall: New York (2001).909 (2007)
46. F. Menil, V. Coillard, and C. Lucat, *Sens. Actuators B* **67**, 1 (2000).

47. M. Stankova, X. Vilanova, E. Llobet, J. Calderer, C. Bittencourt, J. J. Pireaux, and X. Correig, *Sens. Actuators B* **123**, 271 (2005).
48. G. Xie, J. Yu, X. Chen, and Y. Jiang, *Sens. Actuators B* **123**, 909 (2007).
49. S. Santucci, C. Cantalini, M. Crivellari, L. Lozzi, L. Ottaviano, and M. Passacantano, *J. Vac. Sci. Technol. A* **18**, 1007 (2000).
50. R. S. Vemuri, G. Carbajal-Franco, D. A. Ferrer, M. H. Engelhard, C. V. Ramana, *Applied Surface Science* **259**, 172-177 (2012).
51. R. S. Vemuri, M. H. Engelhard, and C. V. Ramana, *Appl. Mater. Interfaces* **4**, 1371-1377 (2012).
52. S.M. Sze, K.K. Ng, *Physics of Semiconductor Devices*, New Jersey: WILEY (2007).
53. M. Hoffman, S. Martin, W. Choi, and D. Bahnemann, *Environmental applications of semiconductor photo catalysis*, *Chemical Review* **95**, 69-96 (1995).
54. University of Cambridge, *Direct and Indirect Band Gap Semiconductors* (2013).
<http://www.doitpoms.ac.uk/tlplib/semiconductors/direct.php>
55. K. Kamala Bharathi, M. Noor-A-Alam, R. S. Vemuri, and C. V. Ramana, *RSC Adv.* **2**, 941 (2012).
56. W. Sahle, M. Nygren, *Journal of Solid State Chemistry* **48** (1983) 154–160.
57. J.M. Berak, M.J. Sienko, *Journal of Solid State Chemistry* **2** (1970) 109–133.
- E. Salje, K. Viswanathan, *Acta Crystallographica A* **31** (1975) 356–359

Curriculum Vita

Amanda P. Christmas (Gutierrez) was born in El Paso, TX. The first and only daughter of Ricardo Gutierrez and Tina L. Gomez. She graduated from Del Valle High School, El Paso, TX in the spring of 2008 and entered the University of Texas at El Paso in the fall of 2008. While pursuing a bachelor's degree in metallurgical and materials engineering, she studied the oxidation effects of niobium alloys through the Office of Naval Research under Dr. S. K. Varma. She also held many officer positions in The Minerals, Metals and Materials Society (TMS), The Society of Women in engineers (SWE), Alpha Sigma Mu (ASMU) and The Engineering Student Leadership Council (ESLC). After graduating in May 2012 she spent the summer interning at Freeport McMoRan Copper and Gold at the Chino Mine in Hurley, NM as a hydrometallurgy engineer. In the fall of 2012, she entered the Graduate School at the University of Texas at El Paso. Under the funding of The National Science Foundation (NSF) and the advisement of Dr. C. V. Ramana she research on W-Ti-O thin films for the applications in photovoltaic devices.

Permanent Address: 5890 Bandolero Dr. #1029
El Paso TX, 79912

Email: apgutierrez@miners.utep.edu